



# Influence of climatic indices (AMO, PDO, and ENSO) and temperature on rainfall in the Northeast Region of India

Ashok Singh<sup>1</sup> · Samir Thakur<sup>1</sup> · Nirab C. Adhikary<sup>2</sup>Received: 17 March 2020 / Accepted: 16 September 2020 / Published online: 23 September 2020  
© Springer Nature Switzerland AG 2020

## Abstract

This study explores the spatiotemporal rainfall variability in the Northeast region of India combined with an analysis of the effects of temperature and natural climatic indices [El-Nino Southern Oscillation (ENSO), Pacific Decadal Oscillation (PDO), and Atlantic Multi-decadal Oscillation (AMO)] on rainfall. The multi-timescale features of rainfall time series for periods 1871–2016 were analysed based on the continuous wavelet transform method. Cross-wavelet and wavelet coherence explore cross-correlation between temperature, natural climatic indices, and rainfall during 1950–2016. Results of the continuous wavelet transform revealed a significant cycle of 12 months on a monthly scale and 2–8-year period on an annual and seasonal scale. The cross-wavelet and wavelet coherence results showed that temperature affects rainfall only on intra-annual (0.5–1 years) scale. ENSO affects rainfall on both intra-annual (0.5–1 years) and inter-annual (1–10 years) scale. PDO affects rainfall on both inter-annual (1–10 years) and decadal (10–21 years) scale. AMO affects rainfall only on the decadal (10–21 years) scale. The result that comes out from this study is useful for climate change assessment, agriculture, and water resources management points of view of the Northeast region of India.

**Keywords** Atlantic Multi-decadal Oscillation (AMO) · El-Nino Southern Oscillation (ENSO) · Northeast region of India · Pacific Decadal Oscillation (PDO)

## 1 Introduction

The climate of a region is the average state of the daily chaotic nonlinear dynamic of the atmosphere. Over the last ten decades, Earth's climate has changed markedly on global and regional scales and characterized by global warming. This change attributes to the combined contribution of the anthropogenic effect and the strong internal mode climate system. El-Nino Southern Oscillation (ENSO), Pacific Decadal Oscillation (PDO), Atlantic Multi-decadal Oscillation (AMO), etc., are among the leading natural climate indices that have a strong impact on global and regional average temperature and rainfall [1, 2].

Several studies throughout the world have reported the impact of these natural climatic phenomena on rainfall

variability [3–9]. Similarly, several authors also reported the significant relationship of Indian rainfall variability with the characteristic oceanic indices [10–14]. In a study, Malik et al. [15] reported that Indian Summer Monsoon rainfall has a consistent negative correlation with PDO. In contrast, its correlation with Total Solar Irradiance and AMO is not stationary on a decadal to multi-decadal scale. In another study, Naidu et al. [16], using sea surface salinity and sea surface temperature data for the last 2000 years of Bay of Bengal, reported that the variability of Indian Summer Monsoon rainfall has modulated with AMO via changes in thermal contrast between the Indian Ocean and Asian landmass.

The Northeast (NE) region of India is a part of Indio-Burma and Himalaya biodiversity hotspots (2 of 35 such

✉ Ashok Singh, ashok11278@yahoo.com | <sup>1</sup>Department of Applied Science, IST, Gauhati University, Guwahati 781014, India. <sup>2</sup>Physical Sciences Division, Institute of Advanced Study in Science and Technology, Paschim Borigaon, Garchuk, Guwahati, Assam 781035, India.



hotspots in the world) [17]. The entire area is encircled by hill and mountain range, whose average height varies from 1 to 5 km. From a meteorological perspective, it is one of the most important regions in the world, containing the world's highest rainfall receiving stations [18, 19]. Average monsoon (June–September) rainfall over this region has recorded highest in the world [20, 21]. Due to the dominant orographic effect, this region has a different rainfall zone, wherein mean annual rainfall varies approximately from 1205 to 12,000 mm [22]. However, in recent decades this region facing the greatest threats from anthropogenic activities and climate change [23, 24]. Further, future climate change projections over this region indicate a significant change in monsoon and winter rainfall [25–27]. Since the rich flora and fauna, some of the most luxuriant forests, power generation, and agricultural production of this region are rain-dependent, any change in the spatial and temporal pattern of rainfall directly affects the biodiversity, rain-fed agriculture ecosystem, and livelihood of its inhabitants.

Understanding the rainfall variability over this region is of particular interest to many researchers from the perspective of agriculture and water resources management. Several researchers reported that the low-pressure area during monsoon season [28–30], local thunderstorm activity [20], and western disturbances [31, 32] are the primary weather system, which is responsible for rainfall variability over this region. Several studies have also noted the statistically increasing/decreasing rainfall trends in monthly and seasonal scale over this region [33–36]. In a study, Preethi et al. [37] reported a declining trend of summer monsoon rainfall of the NE region for the last 4–5 decades. In another study, Prathipati et al. [38] reported a decreasing trend in the frequency of little (less than 20 mm) and moderate (between 20 and 60 mm) rainfall over the NE region. In the context of the attendant effect of oceanic indices on the rainfall variability over the NE region, Prokop et al. [21] reported that the Madden–Julian Oscillation (MJO) plays a potential role in modulating extreme rainfall events during monsoon rainfall over the Meghalaya Hills of the NE region. In another study, Prabhu et al. [39] reported a teleconnection between decreasing trend in summer monsoon rainfall of the NE region with Eurasian snow variability.

Because of the above facts, it is of particular interest to know the effect of natural climatic indices (i.e. ENSO, PDO, and AMO) on the NE region's rainfall variability. Also, the timescales over which these natural climatic indices affect the NE region's rainfall variability remain unclear. Therefore, in this study, we applied wavelet analysis to quantitatively evaluate the spatiotemporal variability of rainfall combined with the effects of natural climatic phenomena (ENSO, PDO, and AMO) on rainfall.

Simultaneously, we try to understand the long-term correlation between the NE region's temperature and rainfall, using different data sets' lengths.

## 2 Data and analytical methods

### 2.1 Data used

The Northeast (NE) region is located in India's eastern-most part, covering an area of 255,036 km<sup>2</sup>. Its latitude extends from 22°00' to 29°30' N and longitude extends from 89°46' to 97°30' E (Fig. 1). Indian Meteorological Department (IMD) divided the entire NE region into five subdivisions as Nagaland–Manipur–Mizoram–Tripura (NMMT), Assam and Meghalaya, Arunachal Pradesh, Sub-Himalayan West Bengal and Sikkim (SHWBS), and Gangetic West Bengal. This present work mainly focuses on analysing the long-term pattern of rainfall and the effect of temperature and climatic indices (ENSO, PDO and AMO) on the rainfall variability of the NE region. The area-weighted monthly rainfall series of NE regions for the period 1871–2016 and 1950–2016 used in this study were prepared by Kothawale and Rajeevan [40], based on the fixed and well-distributed network of 30 rain gauge stations, and the details about the rainfall series are available at the website [https://tropmet.res.in/static\\_pages.php?page\\_id=53](https://tropmet.res.in/static_pages.php?page_id=53). The temperature series of period 1950–2016 used in this study is prepared by using the temperature data sets collected from IITM [41, 42] and the temperature data sets from 29 major weather stations (shown in Fig. 1) gathered from the archive of the National Data Centre [Indian Meteorological Department (IMD)], Pune. The details of the temperature data sets collected from the IITM are available at the website [https://tropmet.res.in/static\\_pages.php?page\\_id=54](https://tropmet.res.in/static_pages.php?page_id=54). The AMO index for the period 1950–2016 (67 years) used in this study obtained from the Earth System Research Laboratory of NOAA [43] is available at the website <https://www.psl.noaa.gov/data/correlation/amon.sm.data>. The PDO index for the period 1950–2016 (67 years) used in this study obtained from the Earth System Research Laboratory of NOAA [44, 45] is available at the website <https://psl.noaa.gov/data/correlation/pdo.data>. The ENSO index for the period 1950–2016 (67 years) used in this study was derived from the SST (Sea Surface Temperature) in the Nino 3.4 region (1200–1700 W, 50 N–50 S) [46] and collected from the Climate Predictor Centre of NOAA are available at the website [http://origin.cpc.ncep.noaa.gov/products/analysis\\_monitoring/ensostuff/detrend.nino34.ascii.txt](http://origin.cpc.ncep.noaa.gov/products/analysis_monitoring/ensostuff/detrend.nino34.ascii.txt).

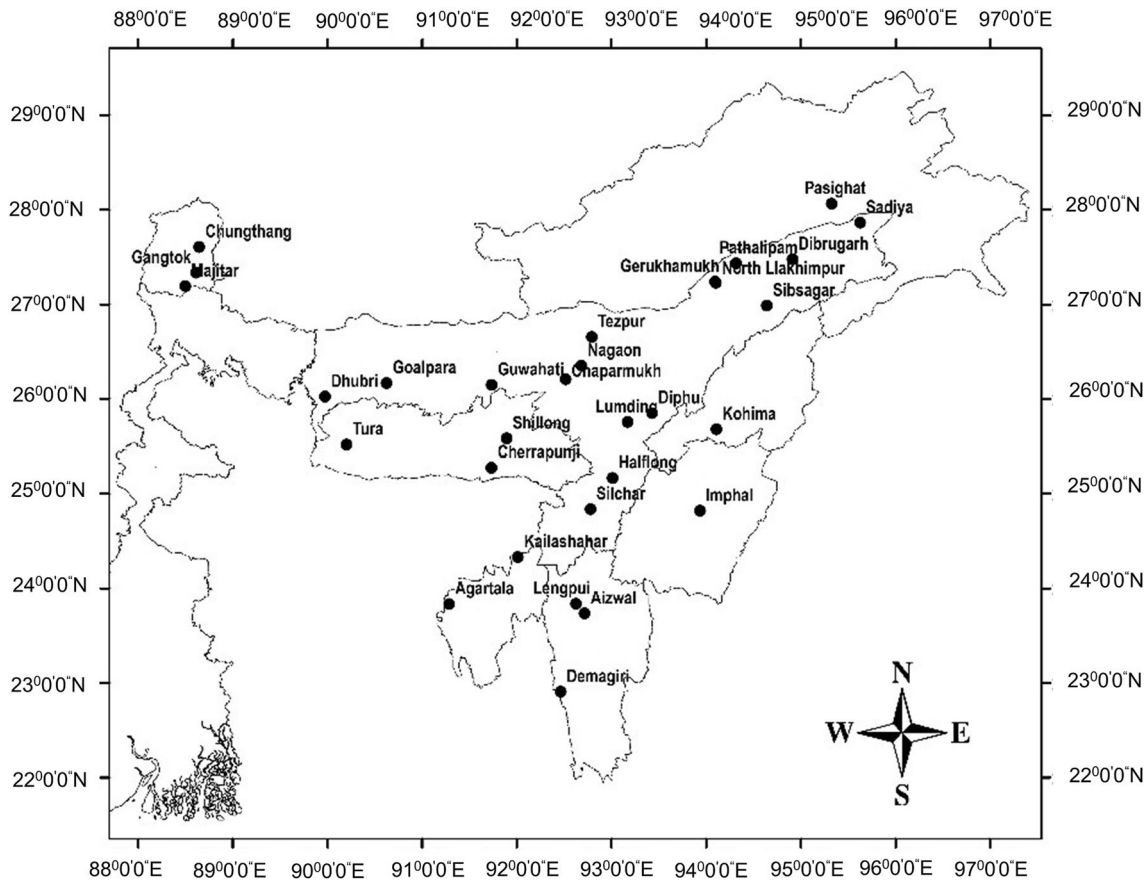


Fig. 1 Location of meteorological stations (IMD) of NE region

### 2.2 Analytical methods

This study utilized wavelet transform (WT) as it is capable of transforming one-dimensional time series into a diffuse two-dimensional and simultaneously provide a time–frequency image. As a result, it is possible to get information on the amplitude of any periodic signals within the series and how it varies with time [47]. To explore the time series multi-timescale feature, complex Morlet wavelet is used as mother wavelet function, defined as:

$$\psi(t) = \pi^{-1/4} e^{iw_0 t} e^{-t^2/2} \tag{1}$$

where  $\psi(t)$  is the wavelet function at non-dimensional time  $t$  and  $w_0$  is the non-dimensional frequency. In this study,  $w_0=6$ , in order to satisfy the admissibility condition; i.e. the function must have zero mean and be localized in both time and frequency space to be admissible as a wavelet [47, 48].

To explore the complete multi-timescale characteristic of the rainfall series, we utilized continuous wavelet transform (CWT) [49]. The edge effects in the wavelet power spectrum have minimized as followed the method

suggested by Torrence and Compo [47]. The significant periodicities detected in the wavelet power spectrum are also confirmed by the global wavelet power spectrum (GWP) at a 5% significant level, assuming red noise. GWP provides an unbiased and consistent estimation of the true power spectrum of the time series [47]. We calculate the scale-average wavelet power spectrum from the wavelet power spectrum to analyse the scale between the dominated periods. The scale-average wavelet power spectrum provides more information about one frequency modulation by another within the same time series [47]. The equations used are as follows:

$$C_x(a, \tau) = \frac{1}{\sqrt{a}} \int_{-\infty}^{+\infty} x(t) \psi_{a,\tau}^* \left( \frac{t-\tau}{a} \right) dt \tag{2}$$

$$W_x(a, \tau) = C_x(a, \tau) C_x^*(a, \tau) = |C_x(a, \tau)|^2 \tag{3}$$

$$\overline{W_x}(a) = \int_{-\infty}^{+\infty} W_x(a, \tau) dt \tag{4}$$

$$a_j = a_0 2^{k\partial_j}, \quad k = 0, 1, \dots, J \tag{5}$$

where  $C_x(a, \tau)$  is the coefficients of wavelet transform of time series  $x(t)$ ,  $\psi_{a,\tau}^*$  is the complex conjugate of mother wavelet  $\psi_{a,\tau}$ ,  $t$  is the integration variable,  $\tau$  is the translation parameter used to slide in time,  $a$  is the dilation parameter used to change the scale,  $W_x(a, \tau)$  is the wavelet power spectrum of signal  $x(t)$ ,  $\overline{W_x(a)}$  is the global wavelet spectrum of signal  $x(t)$ ,  $a_j$  is the scale,  $J$  determines the highest scale, and  $a_0$  is the least resolvable scale. (In this study, we used  $\partial_j = 0.25$ .)

To measure the cross-covariance of climatic indices and rainfall, we used cross-wavelet transform (XWT). Wavelet coherence (WTC) used to detect significant coherence between the time series [50]. The in-phase and out-of-phase relationship between the time series is obtained from the wavelet coherence phase  $\phi_{xy}(a, \tau)$  [51]. The equations used are as follows:

$$W_{xy}(a, \tau) = C_x(a, \tau) C_y^*(a, \tau) \tag{6}$$

$$WC(a, \tau) = \frac{|a^{-1} W_{xy}(a, \tau)|^2}{a^{-1} |W_x(a, \tau)| a^{-1} |W_y(a, \tau)|} \tag{7}$$

$$\phi_{xy}(a, \tau) = \tan^{-1} \left[ \frac{\text{Imaginary part of } W_{xy}(a, \tau)}{\text{Real part of } W_{xy}(a, \tau)} \right] \tag{8}$$

where  $W_{xy}(a, \tau)$  is the wavelet cross-spectrum of signals  $x(t)$  and  $y(t)$ ;  $WC(a, \tau)$  is the wavelet coherence spectrum of signals  $x(t)$  and  $y(t)$ .

All calculations are performed in software R (version 3.5.4) and MATLAB (<http://grinsted.github.io/wavelet-coherence/>).

### 3 Results

#### 3.1 Wavelet analysis of monthly total rainfall

The continuous wavelet transform (CWT) is applied to analyse the rainfall time series. The data used in this study are monthly and yearly distributed. Therefore, the parameter settings are as follows:  $\partial t = 1$  month (or year),  $a_0 = 2\partial t$ ,  $\partial_j = 0.25$  (which will generate 4 sub-octaves per octave),  $j_1 = \frac{7}{\partial_j}$  (which will do 7 power of two with  $\partial_j$  sub-octaves).

Figure 2a demonstrates the monthly total rainfall distribution of the NE region for the period 1871–2016. It can be seen from Fig. 2a that the monthly total rainfall over the

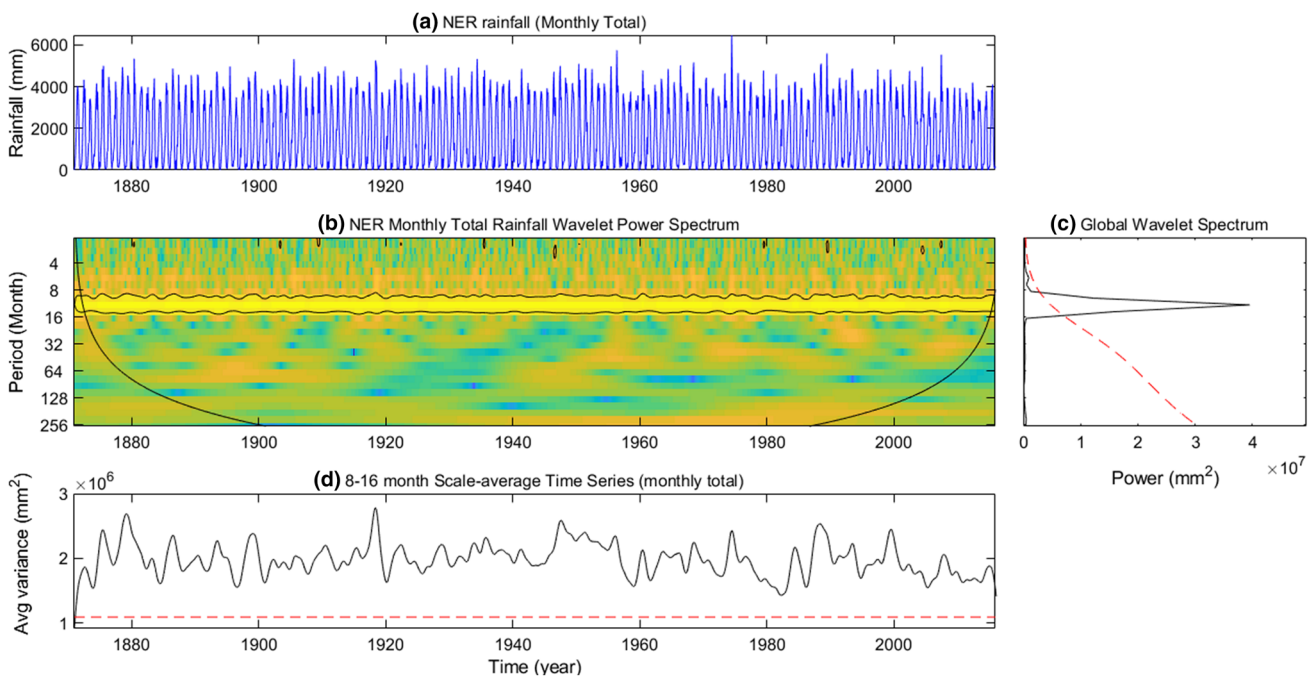


**Fig. 2** **a** Rainfall series of Northeast region 1871–2016. **b** The wavelet power spectrum. The colour in the figure indicates the structure of rainfall variety [the power ranges from strong (dark yellow shades) to weak (deep blue shades)]. The contour level is chosen so that 75%, 50%, 25%, and 5% of wavelet power are above each level, respectively. The region below the black line is the cone of

influence, where zero paddings have reduced the variance. Black contour is the 5% significance level. **c** The global wavelet power spectrum. The dashed line is the 5% significance level for the global wavelet spectrum. **d** Scale-average wavelet power over 8–16-month band for monthly value and 2–8 years for annual value. The dashed line is the 95% confidence level assuming red noise

study region fluctuates in the range from 0.0 to 6463 mm, with a mean monthly total throughout 146 years is 1706.3 mm. Figure 2b depicts the wavelet power spectrum of monthly total rainfall over a range of periods from 2 to 256 months (i.e. frequency from 0.00390625 to 0.5 cycles/month). It is revealed in Fig. 2b that more power in the wavelet power spectrum has concentrated between 8- and 16-month periods. It means this time series has a strong annual signal (12-month periodicity), which is also confirmed by GWP with one important peak almost significant at the 5% level (Fig. 2c).

### 3.2 Wavelet analysis of annual and seasonal rainfall

The annual and seasonal rainfall distributions of the NE region for the period 1871–2016 are shown in Figs. 3a, 4a, 5a, 6a, and 7a, respectively. The wavelet power spectrum of annual (Fig. 3b) and seasonal (Figs. 4b, 5b, 6b, 7b) rainfall series shows a strong periodicity of 2–8 years, wherein most of the power has concentrated. The observed annual and seasonal periodicity 2–8 years has non-consistent throughout 146 years. In the monsoon season, the periodicity 2–8 years has existed during the years 1871–1927 and 1953–2016, and in between the time interval of 25 years, there is no significant periodic

behaviour (Fig. 5b). Another periodicity 2–3 years is only observed in the post-monsoon season (Fig. 6b). All the dominant periodicities (2–8 and 2–3 years) in annual and seasonal rainfall series of wavelet power spectrum have confirmed by GWP with a 95% confidence level (Figs. 3c, 4c, 5c, 6c, 7c). The modulation of one frequency by another within the same time series (i.e. periodicity 2–8 years) has examined using scale-average wavelet power. The scale-average wavelet power has constructed by the average over all the scales between 2 and 8 years of the wavelet power spectrum, which depicted average year variance versus time (Figs. 3d, 4d, 5d, 6d, 7d). The scale-average plot showed some distinct periods when rainfall variance was low, e.g. 1878–1888 and 1923–1951 in annual (Fig. 3d), 1963–1972 in pre-monsoon season (Fig. 4d), 1924–1953 in monsoon (Fig. 5d), 1923–1933 in post-monsoon (Fig. 6d), and 1974–1989 in winter (Fig. 7d). This time interval has identified as a dry period, i.e. rainfall occurred within that period was lower than normal. Similarly, periods wetter than normal years also identified, which indicates by the peak in scale-average time series, e.g. 1972, 1896, 1991, and 2007 in annual (Fig. 3d); 1950 and 1978 in pre-monsoon (Fig. 4d); 1918 and 1993 in monsoon (Fig. 5d); 1971, 1895, and 1986 in post-monsoon (Fig. 6d); and 1875, 1947, and 1956 in winter (Fig. 7d).

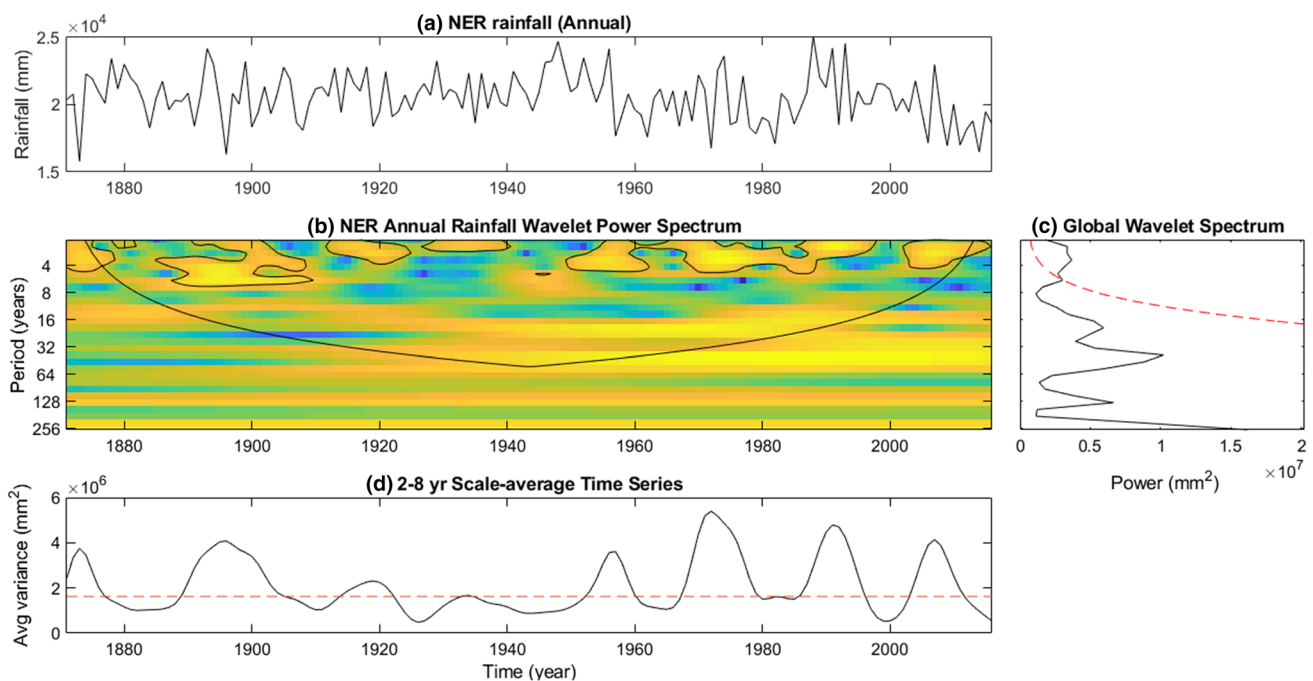


**Fig. 3** **a** Rainfall series of Northeast region 1871–2016. **b** The wavelet power spectrum. The colour in the figure indicates the structure of rainfall variety [the power ranges from strong (dark yellow shades) to weak (deep blue shades)]. The contour level is chosen so that 75%, 50%, 25%, and 5% of wavelet power are above each level, respectively. The region below the black line is the cone of

influence, where zero paddings have reduced the variance. Black contour is the 5% significance level. **c** The global wavelet power spectrum. The dashed line is the 5% significance level for the global wavelet spectrum. **d** Scale-average wavelet power over 8–16-month band for monthly value and 2–8 years for annual value. The dashed line is the 95% confidence level assuming red noise

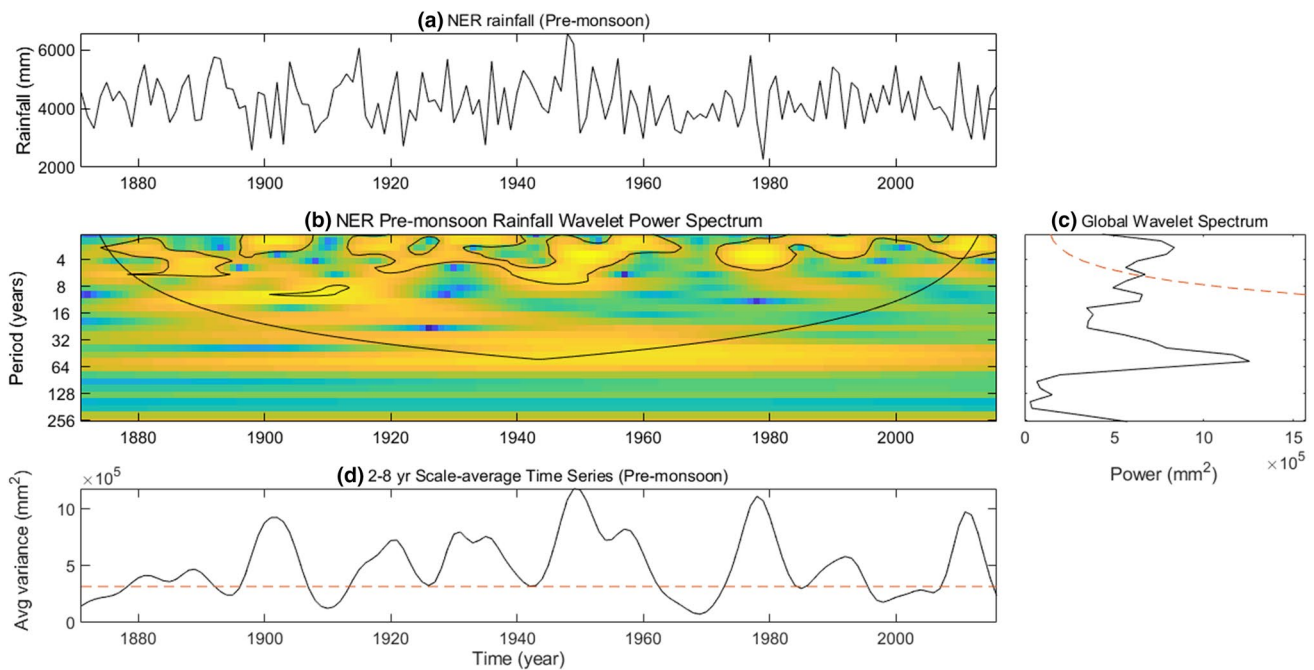


**Fig. 4** **a** Rainfall series of Northeast region 1871–2016. **b** The wavelet power spectrum. The colour in the figure indicates the structure of rainfall variety [the power ranges from strong (dark yellow shades) to weak (deep blue shades)]. The contour level is chosen so that 75%, 50%, 25%, and 5% of wavelet power are above each level, respectively. The region below the black line is the cone of

influence, where zero paddings have reduced the variance. Black contour is the 5% significance level. **c** The global wavelet power spectrum. The dashed line is the 5% significance level for the global wavelet spectrum. **d** Scale-average wavelet power over 8–16-month band for monthly value and 2–8 years for annual value. The dashed line is the 95% confidence level assuming red noise

### 3.3 XWT and WTC between temperature and rainfall

To get the information of correlation between temperature and rainfall in time–frequency domains, cross-wavelet transform (XWT) and wavelet coherence (WTC) have been calculated. We also calculated a significant test against red noise. Figure 8a depicts the cross-wavelet spectrum between monthly mean temperature and monthly total rainfall. It is revealed from Fig. 8a that the temperature and rainfall series correlate closely at high-frequency (periods of 8–16 months) region with high average cross-wavelet power (1.25) throughout the entire range of measurement. Other significant correlations have been observed in high-frequency (periods of 4–8 months) and low-frequency (periods of 162–335 months) regions with average cross-wavelet power of 0.32 and 0.06. Figure 8b demonstrates the actual significant coherence area. The white contour in the wavelet coherence spectrum indicates significant correlation regions. Arrows in the cross-wavelet transform and wavelet coherence have represented the phase difference between temperature and rainfall. In the significantly correlated area (i.e. periods of 8–16 months), all the phase arrows are towards right. It means that the phase difference between temperature and rainfall is equal to 0°, i.e.

the temperature and rainfall series are in phase lock. However, we observed change in behaviour in frequency band 4–8 months and 162–335 months, where all most all the phase arrows have shifted towards left, i.e. both the time series is out of phase or uncorrelated.

### 3.4 XWT and WTC between PDO index and rainfall

Figure 9a, b demonstrates the results of XWT and WTC between the PDO index and monthly total rainfall. The result reveals several statistically significant coherence for both the low- and high-frequency variations (Fig. 9). A closed relationship has been found for the PDO index in high-frequency (8–16 months) region for the short-term intervals (1950–1957, 1985–1992) with high average cross-wavelet power (0.75) having synphase character with a phase difference of 0°. Another phase-lock relationship has observed in the mid-frequency (periods of 26–32 months) region with average cross-wavelet power of 0.25 during 1991–1997. In the mid-frequency (periods of 32–64 months) region, the degree of the relationship was low (0.18) and coherence was synphase during 1975–1985 and antiphase during 1953–1959. In the low-frequency (periods of 64–128 months) region, an antiphase character has observed with low

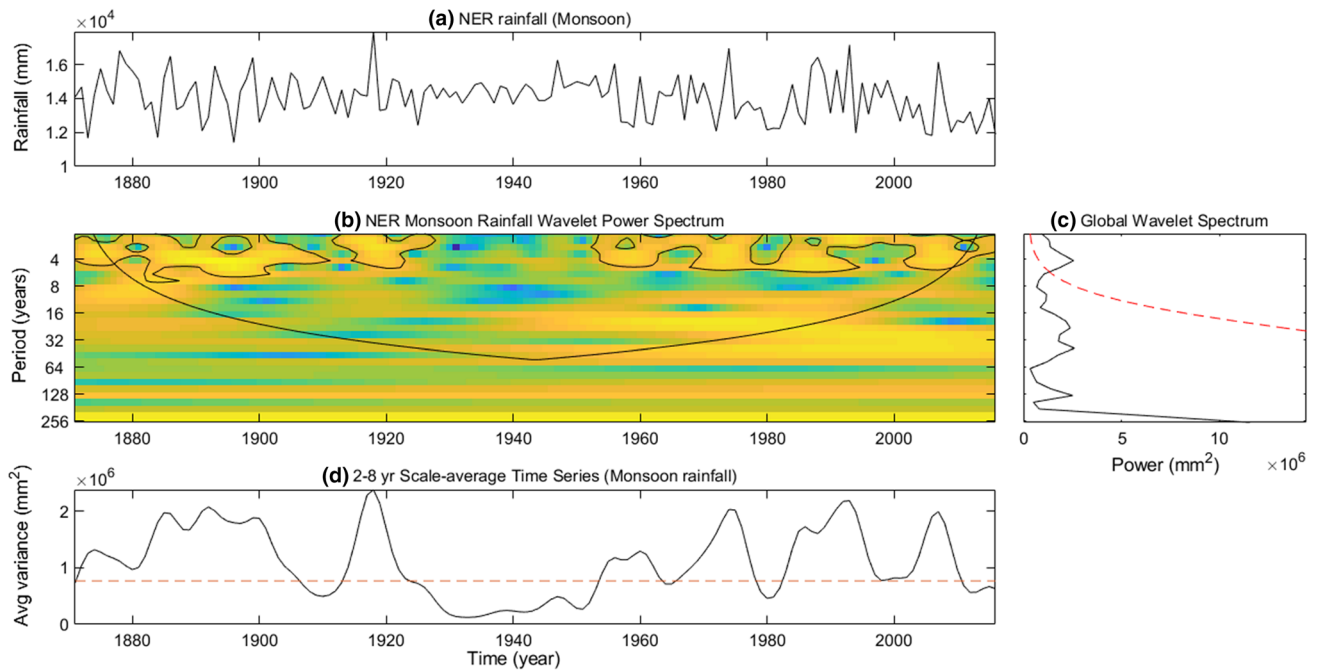


**Fig. 5** **a** Rainfall series of Northeast region 1871–2016. **b** The wavelet power spectrum. The colour in the figure indicates the structure of rainfall variety [the power ranges from strong (dark yellow shades) to weak (deep blue shades)]. The contour level is chosen so that 75%, 50%, 25%, and 5% of wavelet power are above each level, respectively. The region below the black line is the cone of

influence, where zero paddings have reduced the variance. Black contour is the 5% significance level. **c** The global wavelet power spectrum. The dashed line is the 5% significance level for the global wavelet spectrum. **d** Scale-average wavelet power over 8–16-month band for monthly value and 2–8 years for annual value. The dashed line is the 95% confidence level assuming red noise

average cross-wavelet power (0.13) localized between 1988 and 2003. Another antiphase characteristic has also observed in low-frequency oscillation (periods of 128–256 months) with low average cross-wavelet power (0.13) during 1976–2001.

### 3.5 XWT and WTC between AMO index and rainfall

Figure 10a, b demonstrates the result of XWT and WTC between the AMO index and monthly total rainfall. It can be seen from Fig. 10a that the revealed coherence of AMO index and rainfall is stronger in the high-frequency (periods of 8–16 months) region during 1950–2016 and low-frequency (periods of 179–358 months) region during 1960–2006 with high average cross-wavelet power 0.56. Other significant coherence areas have observed in the frequency band 32–128 months. The phase arrows in the low-frequency (periods of 179–358 months) region during 1960–2006 revealed a negative correlation between the AMO index and rainfall with a phase difference  $180^\circ$ , whereas in high-frequency (periods of 8–16 months) region during 1950–2016, phase arrows revealed alternate in-phase and out-phase character for a very short interval of time.

### 3.6 XWT and WTC between ENSO index and rainfall

Figure 11a, b demonstrates the result of XWT and WTC between the ENSO index and monthly total rainfall. The results revealed synphase character of oscillation in the high-frequency (periods of 8–16 months) region with high average cross-wavelet power (0.89) during 1950–2016. An antiphase character of oscillation has also observed in high-frequency (periods of 4–8 months) region with low average cross-wavelet power (0.25) over the entire range of measurement. In the mid-frequency region (periods of 32–64 months), the phase arrows in the significant area show antiphase character with average cross-wavelet power of 0.25 during 1967–1972. Furthermore, in the mid-frequency (periods of 16–64 months) region, we observed five cycles with average cross-wavelet power of 0.25. The phase arrows of the significant area of mid-frequency region (periods of 16–64 months) show that ENSO leads to rainfall (antiphase) during interval 1983–1989, rainfall leads to ENSO (antiphase) during 1953–1960 and ENSO leads to rainfall during 2006–2012 with phase angle  $90^\circ$ . The phase arrows in the low-frequency region (periods of 128–256 months) reveal an antiphase character with meagre cross-wavelet power (0.12) localized in 1980–1997.

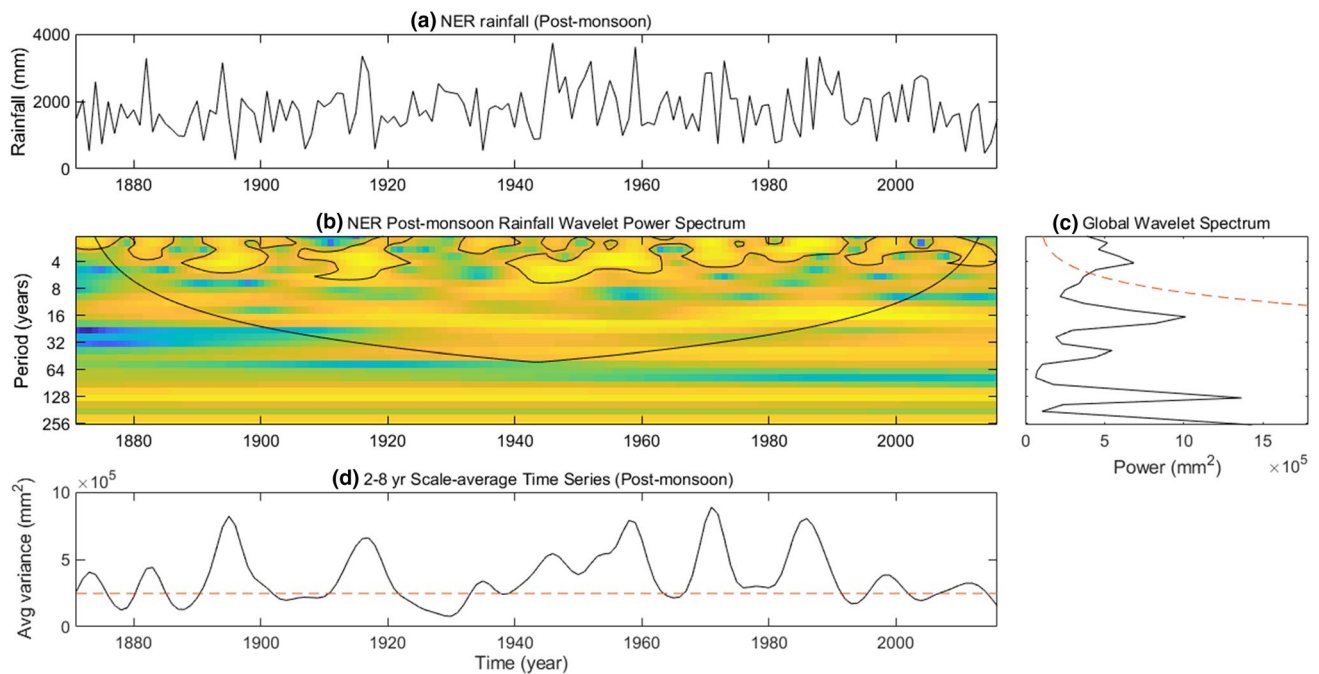


**Fig. 6** **a** Rainfall series of Northeast region 1871–2016. **b** The wavelet power spectrum. The colour in the figure indicates the structure of rainfall variety [the power ranges from strong (dark yellow shades) to weak (deep blue shades)]. The contour level is chosen so that 75%, 50%, 25%, and 5% of wavelet power are above each level, respectively. The region below the black line is the cone of

influence, where zero paddings have reduced the variance. Black contour is the 5% significance level. **c** The global wavelet power spectrum. The dashed line is the 5% significance level for the global wavelet power spectrum. **d** Scale-average wavelet power over 8–16-month band for monthly value and 2–8 years for annual value. The dashed line is the 95% confidence level assuming red noise

## 4 Discussions

The Northeast region of India is one such region in Indian landmass, which receives a large amount of annual average rainfall with only 10% of seasonal variation [20]. About 80% of its annual rainfall occurs during April–October and 66% during June–September [20, 52]. The monthly total rainfall over this region fluctuates in the range from 0.0 to 6463 mm; an average monthly total throughout 146 years (1871–2016) is 1706.3 mm (Fig. 2a). Correlation results (Fig. 8a) demonstrated that temperature mainly affects rainfall at the 6-month and 12-month scale band (Fig. 8a). In the high-frequency area, phase difference at 12 months is almost 0°, i.e. the increasing temperature tends to enhance water vapour in the atmosphere, which arises from open water bodies and vegetation present over this region [31] and also due to glacier melting in the high Himalayas causes convective lifting leading to rainfall. However, the phase difference at 6 months is unstable, i.e. the increasing temperature may increase or decrease rainfall at this scale. Due to different rainfall mechanisms, this region depicted different amounts of rainfall in a different season. Apart from other rainfall mechanisms (e.g. Bay of Bengal and north-westerly disturbances), the occurring bulk amount rainfall during March–May is also probably

due to the thawing of snow-ice masses that start in the summer in high Himalaya with a gradual rise in temperature and supply enough moisture and potential energy favouring the thermodynamic formation of thunderclouds that release considerable rainfall. In the low-frequency region (periods of 162–335 months), two cycles have detected where phase arrows vary from 120° to 150°, which indicates a lead time of 13–28 years. However, they all are very low in power.

The statistical test of wavelet spectra confirmed a strong periodicity of 12 months on a monthly scale and 2–8 years on an annual and seasonal scale (Figs. 2, 3, 4, 5, 6, 7) with a 5% significance level. The periodicity (2–8 years) in the seasonal and annual rainfall patterns is depicted in Figs. 2b, 3b, 4b, 5b, 6b, and 7b generally agreed with the periodicity of ENSO discussed by Torrence and Compo [47]. Further, the ENSO–ISMR (Indian summer monsoon rainfall) relationship has been discussed by several researchers [53–56]. In the majority of El-Nino years, the ISMR is observed to be below average [54]. Our analysis of the ENSO–rainfall relationship shows the same correlation tendency, as observed in the previous studies [54]. However, during most El-Nino years, the rainfall over this region has observed average or above average, consistent with previous studies [54]. Results of

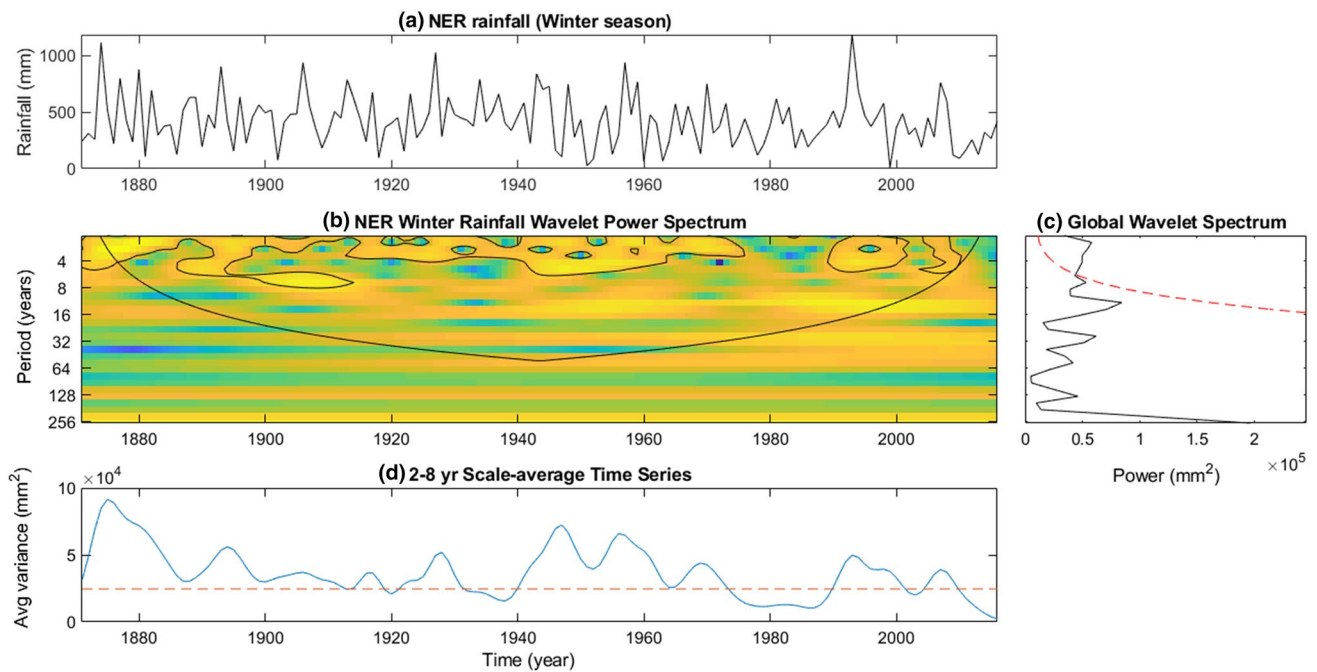


**Fig. 7** **a** Rainfall series of Northeast region 1871–2016. **b** The wavelet power spectrum. The colour in the figure indicates the structure of rainfall variety [the power ranges from strong (dark yellow shades) to weak (deep blue shades)]. The contour level is chosen so that 75%, 50%, 25%, and 5% of wavelet power are above each level, respectively. The region below the black line is the cone of

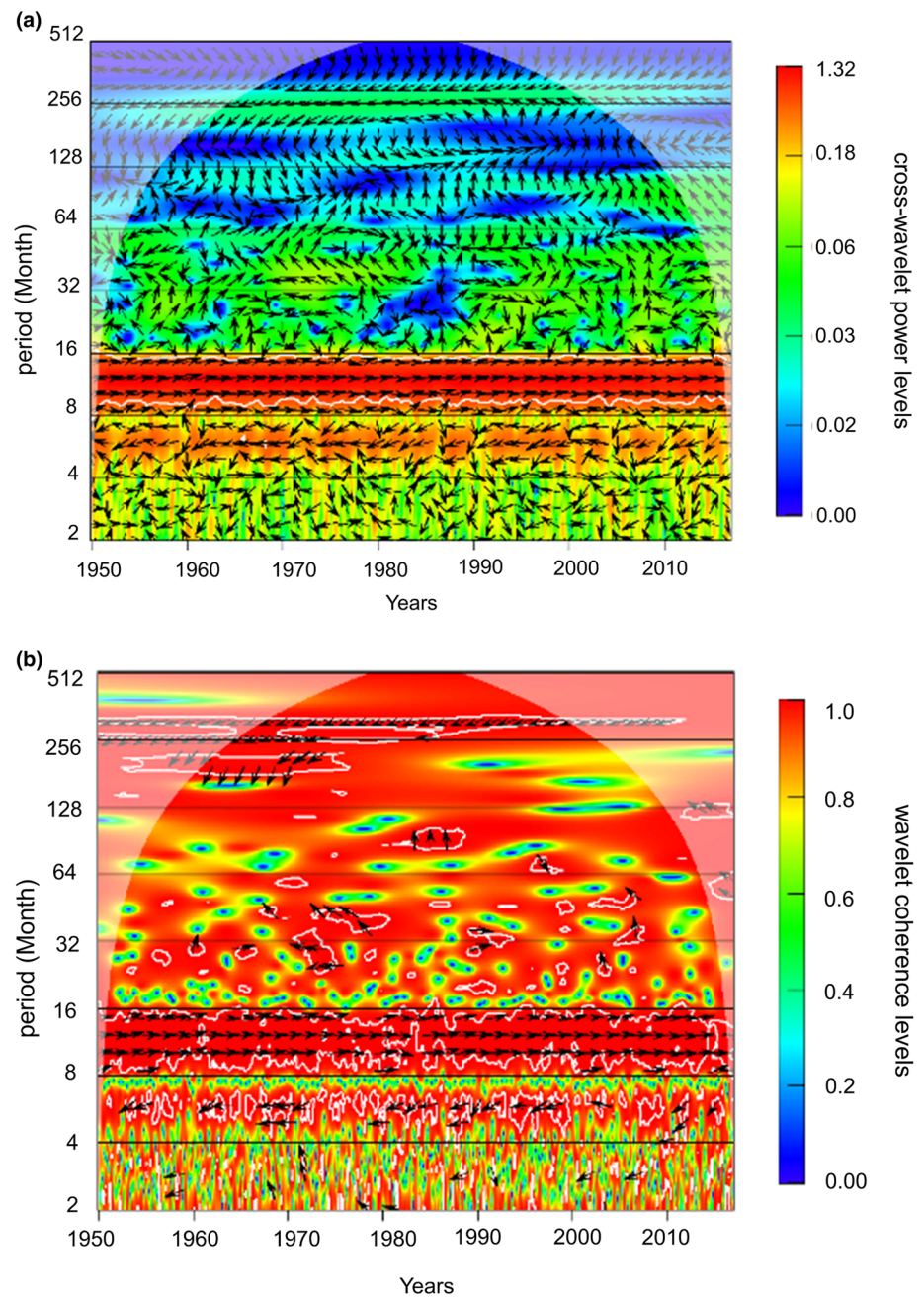
influence, where zero paddings have reduced the variance. Black contour is the 5% significance level. **c** The global wavelet power spectrum. The dashed line is the 5% significance level for the global wavelet spectrum. **d** Scale-average wavelet power over 8–16-month band for monthly value and 2–8 years for annual value. The dashed line is the 95% confidence level assuming red noise

cross-wavelet spectra (Fig. 11b) demonstrated that the ENSO mainly affects the rainfall variability over the NE region on the inter-annual timescale.

The PDO is the pattern of SSTs (Sea Surface Temperatures) in the North Pacific Ocean with periodicities of 15–25 years and 50–70 years [57]. Numerous authors noted the influence of the PDO on the ISMR variability [14, 58, 59]. Krishnan and Sugi [60] noted the occurrence of ISMR below (above) normal when El Niño (La Niña) events occur during positive (negative) phases of the PDO. They explained that the results of the synphase character of PDO and ENSO reinforced SST anomalies, which can alter the convective and dynamical fields, producing persistent anomalies over the tropics and the monsoon region. Our analysis of the PDO–rainfall relationship (Fig. 9a) from the NE region shows a strong correlation on the inter-annual timescale with the average cross-wavelet power of 0.75. However, the correlation between PDO and rainfall on the decadal timescale has very low (0.13). Choudhury et al. [61] also discussed a similar correlation between PDO and monsoon rainfall of the NE region. They noted that the variability of PDO on both inter-annual and inter-decadal timescale is inversely associated with monsoon rainfall over the NE region.

Like PDO, the AMO is the pattern of SSTs in the North Atlantic Ocean with periodicities of 55–80 years [62]. The AMO has been suggested to play a significant role in modulating ISMR on a decadal to a multi-decadal scale [14–16]. In a study, Malik et al. [15], using a long data record of 400 years, reported that the modulation of ISMR on a decadal to multi-decadal scale has influenced by the integrated effect of AMO, PDO, and TSI (Total Solar Irradiance). They noted that most of the dry events (decades) of ISMR occur during the simultaneous negative phase of TSI, the negative phase of AMO, and the positive phase of PDO. Naidu et al. [16], utilizing sea surface salinity ( $\delta^{18}O_w$ ) record of period 2000 years from the Bay of Bengal, reported that the multi-decadal variations of Indian summer rainfall (ISM) influenced by the phase of AMO. The overall increased rainfall over the Indian subcontinent has related to AMO's positive (warm) phase. They also observed a sizeable positive rainfall anomaly over central India and reduced rainfall anomaly over the south and the central Himalayas with a 95% significance level. Krishnamurthy and Krishnamurthy [14] have also observed a similar correlation between AMO and Indian monsoon rainfall (IMR) over central and north India. Our analysis of the AMO–rainfall relationship from the NE region shows a strong correlation on the decadal timescale during the

**Fig. 8** Cross-wavelet spectrum (a) and wavelet coherence (b) between monthly mean temperature and monthly total rainfall. The white contour curves mark the zones with 95% wavelet coherence; the thin curve denotes the boundaries of the influence cone

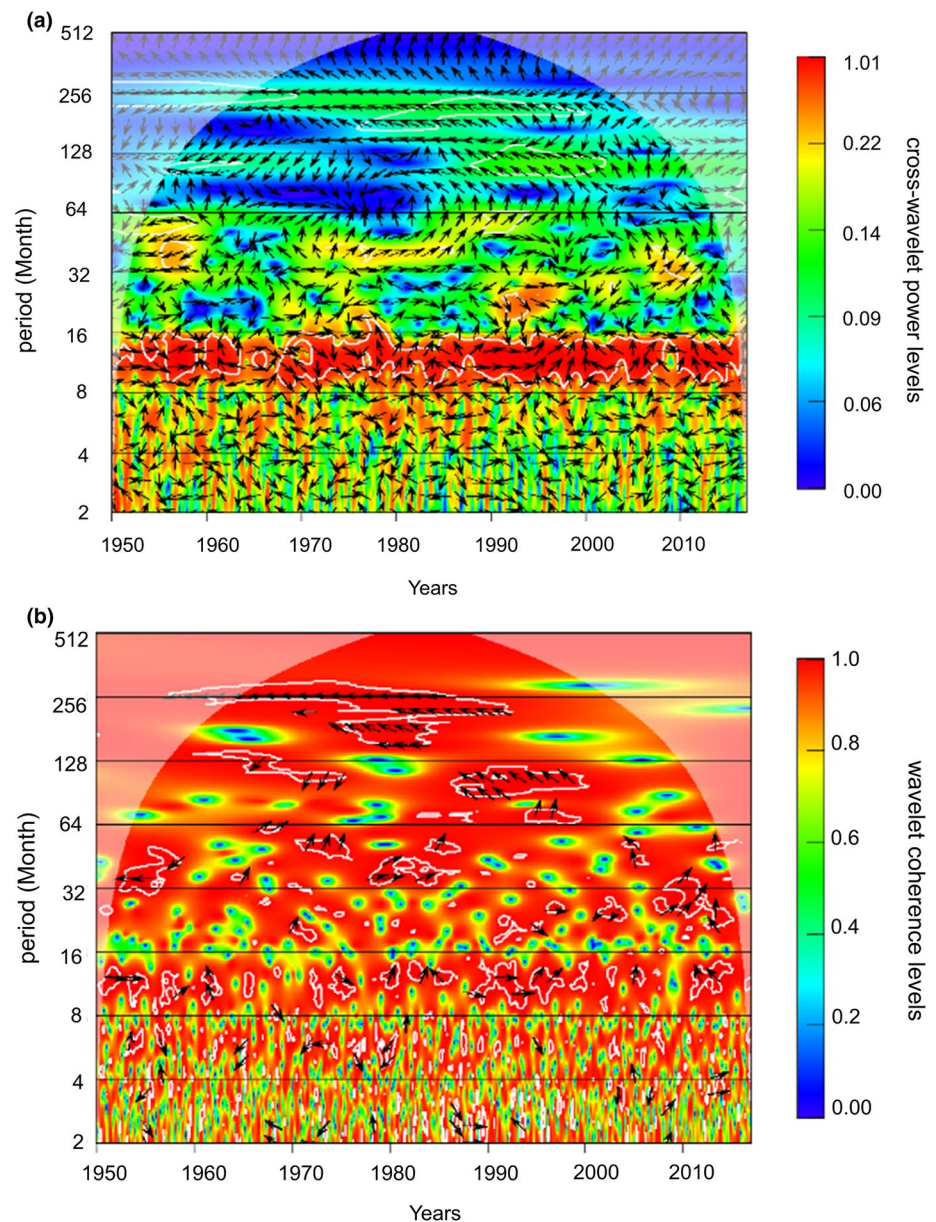


interval 1960–2006 with average cross-wavelet power of 0.56. However, the phase arrows in the significant area in the high-frequency region during 1950–2016 are randomly oriented, so its manifestation is not clear. The correlation between AMO and rainfall variability during 1960–2006 is consistent with Naidu et al. [16]; however, the two records have not precisely matched temporally.

The NE region’s rainfall variability on the temporal scale is the integrated effects of natural climate modes [21, 39, 54, 58, 60]. The seasonal rainfall variability over this region is mainly due to the Indian monsoon system. The heaviest rainfall events during the pre-monsoon season over this

region have suggested to associating with the thunderstorm or local convective activities [20, 31]. The increasing heaviest rainfall events during the monsoon season are some extent associated with the Madden–Julian oscillation [21]. However, the wintertime Eurasian snow variability associated with Arctic Oscillation has been suggested to play a significant role in modulating monsoon rainfall variability [39]. In the inter-annual timescale, this study noted ENSO’s influence on rainfall variability with low average cross-wavelet power. At the same time, the phase of PDO plays a significant role in modulating the ENSO–rainfall relationship. In the decadal timescale, this

**Fig. 9** Cross-wavelet spectrum (a) and wavelet coherence (b) between PDO index and monthly total rainfall. The white contour curves mark the zones with 95% wavelet coherence; the thin curve denotes the boundaries of the influence cone



study observed both PDO and AMO's effect on rainfall variability. However, AMO's effect on rainfall variability in the decadal timescale is more substantial compared to PDO.

## 5 Conclusion

This study utilized CWT, XWT, and WTC to understand the effects of temperature and natural climatic indices (ENSO, PDO, AMO) on the NE region's rainfall variability. The CWT and GWP results revealed the spatiotemporal peculiarities of variations in annual and seasonal

rainfall. The XWT and WTC results revealed the effects of temperature and climatic indices on rainfall variability. The temperature affects rainfall only on intra-annual (0.5–1 year) scale. The ENSO affects rainfall variability on both intra-annual (0.5–1 year) and inter-annual (1–10 years) scale. The PDO affects rainfall variability on both inter-annual (1–10 years) and decadal (10–21 years) scale. The AMO affects rainfall variability only on the decadal (10–21 years) scale at a 5% significant level. The results that come out from this study are significant for the assessment of climate change in the NE region and useful for agricultural and water management.

**Fig. 10** Cross-wavelet spectrum (a) and wavelet coherence (b) between AMO index and monthly total rainfall. The white contour curves mark the zones with 95% wavelet coherence; the thin curve denotes the boundaries of the influence cone

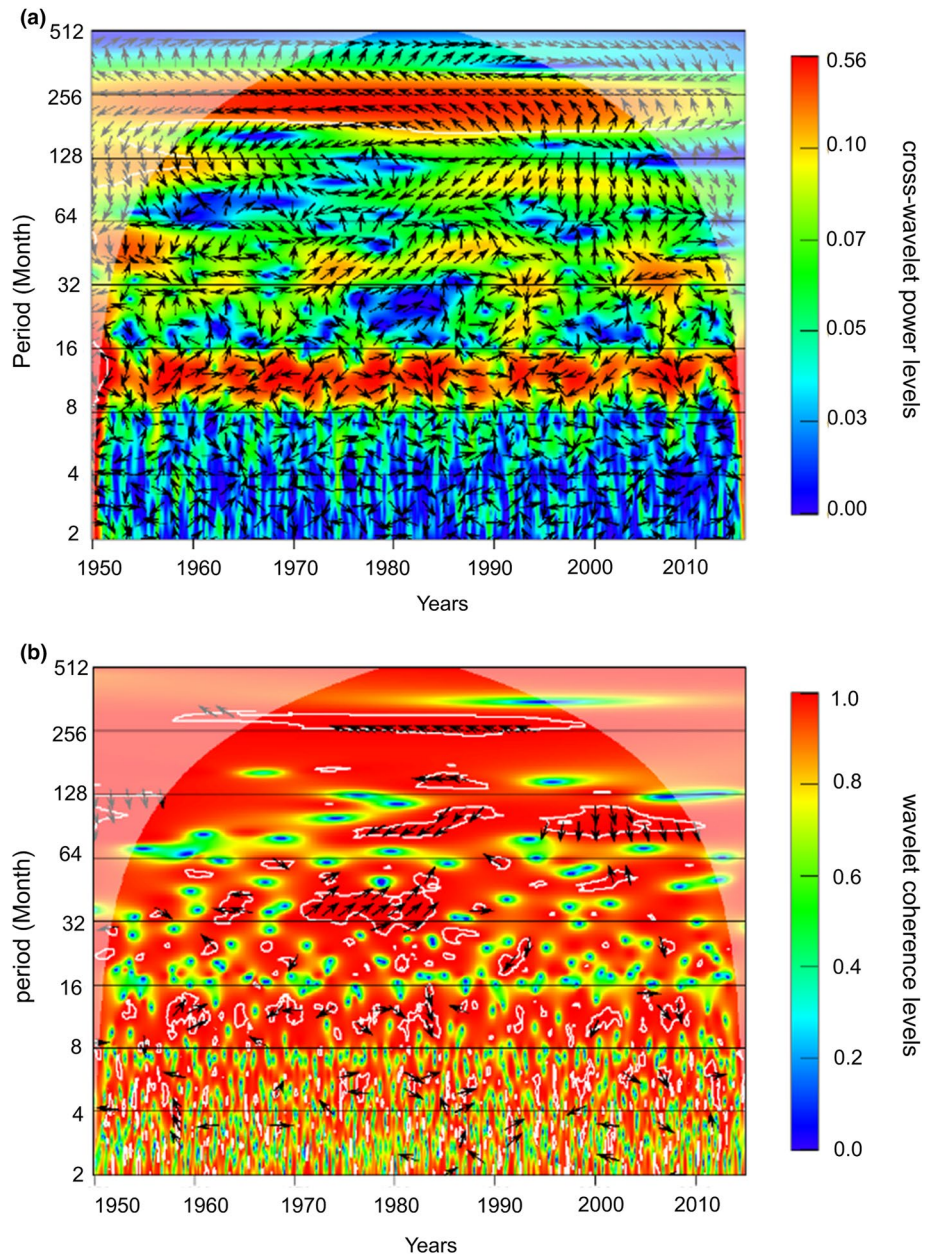
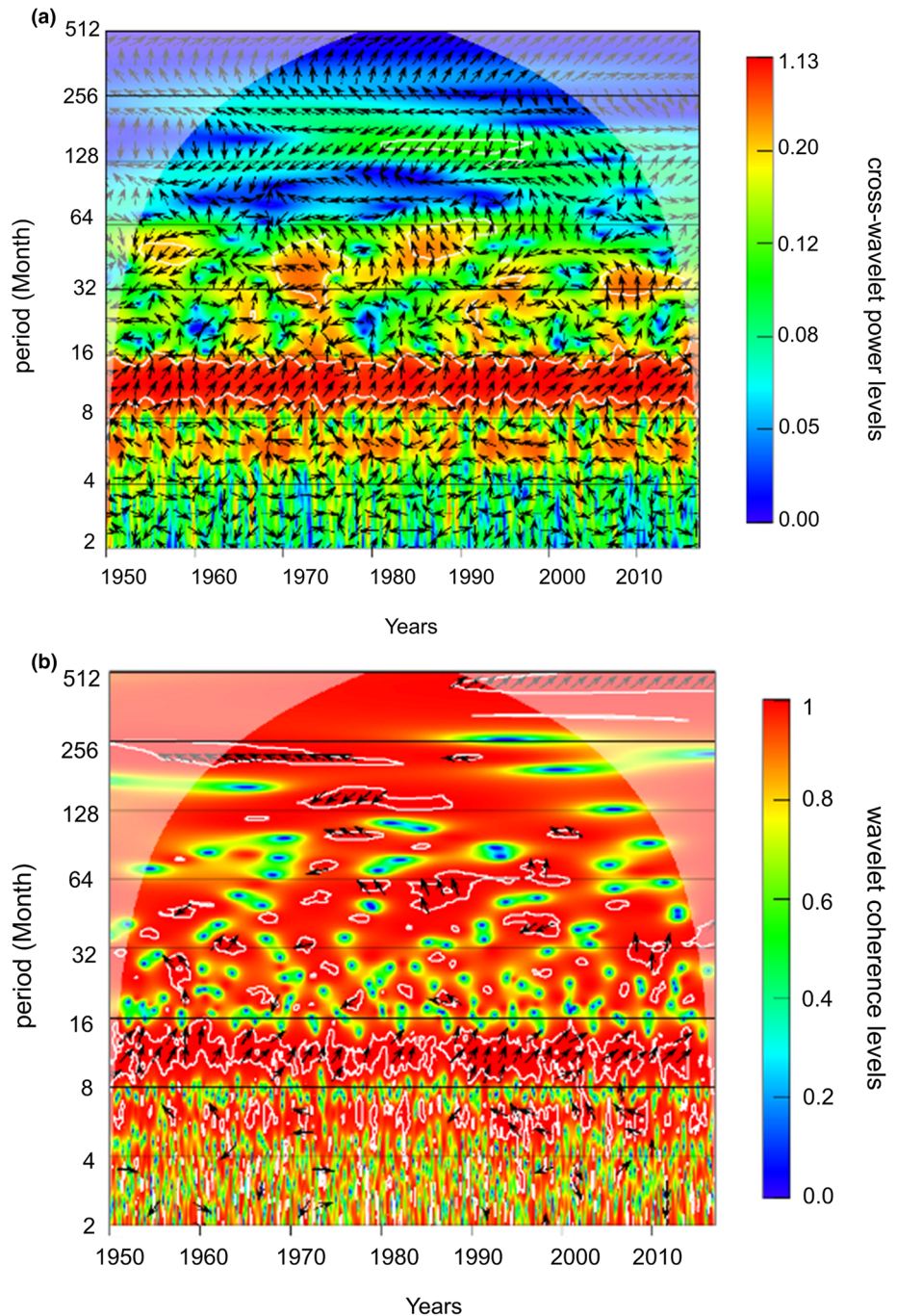


**Fig. 11** Cross-wavelet spectrum (a) and wavelet coherence (b) between ENSO index and monthly total rainfall. The white contour curves mark the zones with 95% wavelet coherence; the thin curve denotes the boundaries of the influence cone



**Acknowledgements** We are thankful to the National Data Center, IMD, Pune, to provide the dataset for the research. Further, we would also like to thank the Physical Science division Department of Applied Sciences, Gauhati University, and Physical Sciences Division, IASST, Guwahati, for providing the computing facility and their generous support. The authors also thankful to Dr. Eeshankur Saikia, Physical Science Division, Department of Applied Sciences, Gauhati University for his valuable suggestions.

### Compliance with ethical standards

**Conflict of interest** On behalf of all authors, the corresponding author states that there is no conflict of interest.

## References

- Sutton RT (2005) Atlantic Ocean forcing of North American and European Summer climate. *Science* 309:115–118. <https://doi.org/10.1126/science.1109496>
- Li S, Bates GT (2007) Influence of the Atlantic multidecadal oscillation on the winter climate of East China. *Adv Atmos Sci* 24:126–135. <https://doi.org/10.1007/s00376-007-0126-6>
- Chan JCL, Zhou W (2005) PDO, ENSO and the early summer monsoon rainfall over south China. *Geophys Res Lett* 32:L08810. <https://doi.org/10.1029/2004gl022015>
- Zhang R, Delworth TL (2006) Impact of Atlantic multidecadal oscillations on India/Sahel rainfall and Atlantic hurricanes. *Geophys Res Lett* 33:L17712. <https://doi.org/10.1029/2006gl026267>
- Krishnamurthy L, Krishnamurthy V (2013) Influence of PDO on South Asian summer monsoon and monsoon–ENSO relation. *Clim Dyn* 42(9–10):2397–2410. <https://doi.org/10.1007/s00382-013-1856-z>
- Chansaengkrachang K, Luadsong A, Ascharyapho N (2014) A study of the time lags of the Indian Ocean dipole and rainfall over Thailand by using the cross wavelet analysis. *Arab J Sci Eng* 40:215–225. <https://doi.org/10.1007/s13369-014-1480-1>
- Xiao MZ, Zhang Q, Singh VP (2015) Influences of ENSO, NAO, IOD and PDO on seasonal precipitation regimes in the Yangtze River Basin, China. *Int J Climatol* 35:2556–3567. <https://doi.org/10.1002/joc.4228>
- Chang X, Wang B, Yan Y, Hao Y, Zhang M (2018) Characterizing effects of monsoons and climate teleconnections on precipitation in China using wavelet coherence and global coherence. *Clim Dyn* 52:5213–5228. <https://doi.org/10.1007/s00382-018-4439-1>
- De la Casa AC, Ovando GG, Díaz GJ (2019) Interannual variability of seasonal rainfall in Cordoba, Argentina, evaluated from ENSO and ENSO Modoki signals and verified with MODIS NDMI data. *SN Appl Sci* 1:1624. <https://doi.org/10.1007/s42452-019-1650-6>
- Kripalani RH, Kulkarni A (1997) Climatic impact of El Niño/La Niña on the Indian monsoon: a new perspective. *Weather* 52(2):39–46. <https://doi.org/10.1002/j.1477-8696.1997.tb06267.x>
- Kumar KK, Rajagopalan B, Cane MA (1999) On the weakening relationship between the Indian monsoon and ENSO. *Science* 284(5423):2156–2159. <https://doi.org/10.1126/science.284.5423.2156>
- Kucharski F, Bracco A, Yoo JH, Molteni F (2007) Low-frequency variability of the Indian monsoon–ENSO relationship and the tropical Atlantic: the “Weakening” of the 1980s and 1990s. *J Clim* 20:4255–4266. <https://doi.org/10.1175/jcli4254.1>
- Li S, Perlwitz J, Quan X, Hoerling MP (2008) Modelling the influence of North Atlantic multidecadal warmth on the Indian summer rainfall. *Geophys Res Lett* 35:L05804. <https://doi.org/10.1029/2007gl032901>
- Krishnamurthy L, Krishnamurthy V (2015) Teleconnections of Indian monsoon rainfall with AMO and Atlantic tripole. *Clim Dyn* 46:2269–2285. <https://doi.org/10.1007/s00382-015-2701-3>
- Malik A, Brönnimann S, Stickler A, Raible CC, Muthers S, Anet J, Rozanov E, Schmutz W (2017) Decadal to multi-decadal scale variability of Indian summer monsoon rainfall in the coupled ocean–atmosphere–chemistry climate model SOCOL-MPIOM. *Clim Dyn* 49(9–10):3551–3572. <https://doi.org/10.1007/s00382-017-3529-9>
- Naidu PD, Ganeshram R, Bollasina MA, Panmei C, Nürnberg D, Donges JF (2020) Coherent response of the Indian monsoon rainfall to Atlantic multi-decadal variability over the last 2000 years. *Sci Rep*. <https://doi.org/10.1038/s41598-020-58265-3>
- Sivaperuman C, Venkataraman K (eds) (2018) Indian hotspots. Springer, Singapore. <https://doi.org/10.1007/978-981-10-6605-4>
- Dhar ON, Farooqui SMT (1973) A study of rainfalls recorded at the Cherrapunji observatory. *Hydrol Sci Bull* 18:441–450. <https://doi.org/10.1080/02626667309494059>
- Oliver JE, Hidore JJ (2003) *Climatology—an atmospheric science*. Pearson Education (Singapore) Ptc. Ltd, p 177
- Mahanta R, Sarma D, Choudhury A (2012) Heavy rainfall occurrences in northeast India. *Int J Climatol* 33:1456–1469. <https://doi.org/10.1002/joc.3526>
- Prokop P, Walanus A (2014) Variation in the orographic extreme rain events over the Meghalaya Hills in northeast India in the two halves of the twentieth century. *Theor Appl Climatol* 121:389–399. <https://doi.org/10.1007/s00704-014-1224-x>
- Murata F, Terao T, Hayashi T, Asada H, Matsumoto J (2008) Relationship between atmospheric conditions at Dhaka, Bangladesh, and rainfall at Cherrapunjee, India. *Nat Hazards* 44:399–410. <https://doi.org/10.1007/s11069-007-9125-2>
- Ravindranath NH, Rao S, Sharma N, Nair M, Gopalakrishnan R, Rao AS, Malaviya S, Tiwari R, Sagadevan A, Munsri M, Krishna N, Bala G (2011) Climate change vulnerability profiles for North East India. *Curr Sci (Bangalore)* 101(3):384–394
- Osipova E, Shadie P, Zwahlen C, Osti M, Shi Y, Kormos C, Bertzky B, Murai M, Van Merm R, Badman T (2017) IUCN World Heritage Outlook 2: a conservation assessment of all natural World Heritage sites. IUCN, Gland, p 92
- Rupa kumar K, Sahai AK, Kumar KK, Patwardhan SK, Mishra PK, Revadekar JV, Kamala K, Pant GB (2006) High-resolution climate change scenarios for India for the 21st century. *Curr Sci* 90(3):334–345
- Rajendran K, Kitoh A (2008) Indian summer monsoon in future climate projection by a super high-resolution global model. *Curr Sci* 95:1560–1569
- Kulkarni A, Kripalani RH, Sabada SS (2010) Examining Indian monsoon variability in coupled climate model simulation and projection. IITM Research Report RR 125
- Medina S, Houze RA, Kumar A, Niyogi D (2010) Summer monsoon convection in the Himalayan region: terrain and land cover effects. *Q J R Meteorol Soc* 136:593–616. <https://doi.org/10.1002/qj.601>
- Goswami BB, Mukhopadhyay P, Mahanta R, Goswami BN (2010) Multiscale interaction with topography and extreme rainfall events in the northeast Indian region. *J Geophys Res*. <https://doi.org/10.1029/2009jd012275>
- Breitenbach SFM, Adkins JF, Meyer H, Marwan N, Kumar KK, Haug GH (2010) Strong influence of water vapor source dynamics on stable isotopes in precipitation observed in Southern Meghalaya, NE, India. *Earth Planet Sci Lett* 292(1–2):212–220. <https://doi.org/10.1016/j.epsl.2010.01.038>
- Pradhan R, Singh N, Singh RP (2019) Onset of summer monsoon in Northeast India is preceded by enhanced transpiration. *Sci Rep*. <https://doi.org/10.1038/s41598-019-55186-8>
- Dimri AP, Niyogi D, Barros AP, Ridley J, Mohanty UC, Yasunari T, Sikka DR (2015) Western disturbances: a review. *Rev Geophys* 53:225–246. <https://doi.org/10.1002/2014rg000460>
- Jain SK, Kumar V, Saharia M (2012) Analysis of rainfall and temperature trends in northeast India. *Int J Climatol* 33:968–978. <https://doi.org/10.1002/joc.3483>
- Jhajharia D, Yadav BK, Maske S, Chattopadhyay S, Kar AK (2012) Identification of trends in rainfall, rainy days and 24 h maximum rainfall over subtropical Assam in Northeast India. *C R Geosci* 344:1–13. <https://doi.org/10.1016/j.crte.2011.11.002>
- Deka RL, Mahanta C, Pathak H et al (2012) Trends and fluctuations of rainfall regime in the Brahmaputra and Barak basins of Assam, India. *Theor Appl Climatol* 114:61–71. <https://doi.org/10.1007/s00704-012-0820-x>

36. Goyal MK (2014) Statistical analysis of long term trends of rainfall during 1901–2002 at Assam, India. *Water Resour Manage* 28(6):1501–1515. <https://doi.org/10.1007/s11269-014-0529-y>
37. Preethi B, Mujumdar M, Kripalani RH, Prabhu A, Krishnan R (2016) Recent trends and tele-connections among South and East Asian summer monsoons in a warming environment. *Clim Dyn* 48:2489–2505. <https://doi.org/10.1007/s00382-016-3218-0>
38. Prathipati VK, Naidu CV, Konatham P (2019) Inconsistency in the frequency of rainfall events in the Indian summer monsoon season. *Int J Climatol* 39:4907–4923. <https://doi.org/10.1002/joc.6113>
39. Prabhu A, Oh J, Kim I, Kripalani RH, Mitra AK, Pandithurai G (2016) Summer monsoon rainfall variability over North East regions of India and its association with Eurasian snow, Atlantic Sea Surface temperature and Arctic Oscillation. *Clim Dyn* 49:2545–2556. <https://doi.org/10.1007/s00382-016-3445-4>
40. Kothawale DR, Rajeevan M (2017) Monthly, seasonal and annual rainfall time series for all-India, homogeneous regions and meteorological subdivisions: 1871–2016. Research Report No. RR-138, ESSO/IITM/STCVP/SR/02(2017)/189: 1–169
41. Kothawale DR, Rupa Kumar K (2005) On the recent changes in surface temperature trends over India. *Geophys Res Lett* 32:L18714. <https://doi.org/10.1029/2005gl023528>
42. Kothawale DR, Kumar KK, Srinivasan G (2012) Spatial asymmetry of temperature trends over India and possible role of aerosols. *Theor Appl Climatol* 110(1–2):263–280. <https://doi.org/10.1007/s00704-012-0628-8>
43. Enfield DB, Mestas-Nuñez AM, Trimble PJ (2001) The Atlantic Multidecadal Oscillation and its relation to rainfall and river flows in the continental US. *Geophys Res Lett* 28:2077–2080. <https://doi.org/10.1029/2000gl012745>
44. Zhang Y, Wallace JM, Battisti DS (1997) ENSO-like interdecadal variability: 1900–1993. *J Clim* 10(5):1004–1020. [https://doi.org/10.1175/1520-0442\(1997\)010%3c1004:eliv%3e2.0.co;2](https://doi.org/10.1175/1520-0442(1997)010%3c1004:eliv%3e2.0.co;2)
45. Mantua NJ, Hare SR, Zhang Y, Wallace JM, Francis RC (1997) A Pacific interdecadal climate oscillation with impacts on salmon production. *Bull Am Meteorol Soc* 78(6):1069–1079. [https://doi.org/10.1175/1520-0477\(1997\)078%3c1069:apicow%3e2.0.co;2](https://doi.org/10.1175/1520-0477(1997)078%3c1069:apicow%3e2.0.co;2)
46. Huang B, Thorne PW, Banzon VF, Boyer T, Chepurin G, Lawrimore JH, Menne M, Smith T, Vose R, Zhang HM (2017) Extended reconstructed sea surface temperature, version 5 (ERSSTv5): upgrades, validations, and intercomparisons. *J Clim* 30(20):8179–8205. <https://doi.org/10.1175/jcli-d-16-0836.1>
47. Torrence C, Compo GP (1998) A practical guide to wavelet analysis. *Bull Am Meteorol Soc* 79(1):61–78. [https://doi.org/10.1175/1520-0477\(1998\)079%3c0061:apgtwa%3e2.0.co;2](https://doi.org/10.1175/1520-0477(1998)079%3c0061:apgtwa%3e2.0.co;2)
48. Farge M (1992) Wavelet transforms and their applications to turbulence. *Annu Rev Fluid Mech* 24(1):395–458. <https://doi.org/10.1146/annurev.fl.24.010192.002143>
49. Zeri M, Cunha-Zeri G, Gois G, Lyra GB, Oliveira-Júnior JF (2018) Exposure assessment of rainfall to interannual variability using the wavelet transform. *Int J Climatol* 39:568–578. <https://doi.org/10.1002/joc.5812>
50. Liu YC, Zhao K, Liu Y, Yin XL, Labat D (2018) Analysis of the impact of precipitation and temperature on the streamflow of the Ürümqi River, Tianshan Mountain, China. *IOP Conf Ser Earth Environ Sci* 191:12135. <https://doi.org/10.1088/1755-1315/191/1/012135>
51. Grinsted A, Moore JC, Jevrejeva S (2004) Application of the cross wavelet transform and wavelet coherence to geophysical time series. *Nonlinear Process Geophys* 11:561–566
52. Srinivasan V, Raman S, Mukherjee S (1972) South-West monsoon—typical situation over West Bengal and Assam and adjoining states. *IMD FMU Report III* 3.6, 1.67
53. Khandekar ML (1979) Climatic teleconnections from the equatorial Pacific to the Indian monsoon, analysis and implications. *Arch Meteor Geophys Bioclimatol* A28:159–168
54. Mooley DA, Parthasarathy B (1983) Indian summer monsoon and El Niño. *Pure Appl Geophys PAGEOPH* 121:339–352. <https://doi.org/10.1007/bf02590143>
55. Rasmusson EM, Carpenter TH (1983) The relationship between eastern equatorial Pacific Sea surface temperatures and rainfall over India and Sri Lanka. *Mon Weather Rev* 111:517–528. [https://doi.org/10.1175/1520-0493\(1983\)111%3c0517:trbee%3e2.0.co;2](https://doi.org/10.1175/1520-0493(1983)111%3c0517:trbee%3e2.0.co;2)
56. Parthasarathy B, Pant GB (1985) Seasonal relationships between Indian summer monsoon rainfall and the southern oscillation. *J Climatol* 5:369–378. <https://doi.org/10.1002/joc.3370050404>
57. Mantua NJ, Hare ST (2002) The Pacific decadal oscillation. *J Oceanogr* 58(1):35–44. <https://doi.org/10.1023/a:1015820616384>
58. Sen Roy S (2010) Identification of periodicity in the relationship between PDO, El Niño and peak monsoon rainfall in India using S-transform analysis. *Int J Climatol* 31:1507–1517. <https://doi.org/10.1002/joc.2172>
59. Myers CG, Oster JL, Sharp WD, Bennartz R, Kelley NP, Covey AK, Breitenbach SFM (2015) Northeast Indian stalagmite records Pacific decadal climate change: implications for moisture transport and drought in India. *Geophys Res Lett* 42:4124–4132. <https://doi.org/10.1002/2015gl063826>
60. Krishnan R, Sugi M (2003) Pacific decadal oscillation and variability of the Indian summer monsoon rainfall. *Clim Dyn* 21:233–242. <https://doi.org/10.1007/s00382-003-0330-8>
61. Choudhury BA, Saha SK, Konwar M, Sujith K, Deshamukhya A (2019) Rapid drying of Northeast India in the last three decades: climate change or natural variability? *J Geophys Res Atmos* 124:227–237. <https://doi.org/10.1029/2018jd029625>
62. Knight JR, Folland CK, Scaife AA (2006) Climate impacts of the Atlantic multidecadal oscillation. *Geophys Res Lett*. <https://doi.org/10.1029/2006gl026242>

**Publisher's Note** Springer Nature remains neutral with regard to jurisdictional claims in published maps and institutional affiliations.